Experimental Mechanics (2016) 56:493–506
DOI 10.1007/s11340-015-0111-4

Shear Characterization of Adhesive Layers by Advanced Optical Techniques

A.C.C. Leitão [1] · R.D.S.G. Campilho [1] · D.C. Moura [2]

Received: 29 June 2015 / Accepted: 10 November 2015 / Published online: 2 December 2015

Abstract With adhesive bonding, design can be oriented towards lighter structures because of the direct weight savings over fastened or welded joints and also due to the flexibility to joint different materials. Cohesive Zone Models (CZM) are a powerful design tool, although the CZM laws of the adhesive bond in tension and shear are required as input in the models. This work experimentally evaluates the shear fracture toughness (G_{IIC}) and CZM laws of bonded joints for three adhesives with distinct ductility. G_{IIC} was characterized by conventional and the *J*-integral techniques. Additionally, by the *J*-integral technique, the precise shape of the cohesive law was defined. For the *J*-integral, a digital image correlation method is used to estimate the adhesive layer shear displacement at the crack tip (δ_s) during the test, coupled to a Matlab® sub-routine for extraction of this parameter automatically. As output of this work, fracture data is provided in shear for each adhesive, showing the marked differences between the three adhesives evaluated. This information enables the subsequent strength prediction of bonded joints under this mode of loading.

Keywords Adhesive joint · Fracture toughness · Cohesive law · Experimental testing · Digital image correlation

✉ R. D. S. G. Campilho
raulcampilho@gmail.com

[1] Departamento de Engenharia Mecânica, Instituto Superior de Engenharia do Porto, Instituto Politécnico do Porto, Rua Dr. António Bernardino de Almeida, 431, 4200-072 Porto, Portugal

[2] Instituto de Telecomunicações, Departamento de Engenharia Electrotécnica e de Computadores, Faculdade de Engenharia, Universidade do Porto, Porto, Portugal

Introduction

Modern and competitive structures are sought to be strong, reliable and lightweight, which increased the industrial and research interest in adhesive bonding, namely improving the materials strength and fracture properties. With this joining technique, design can be oriented towards lighter structures, not only regarding the direct weight saving advantages of the joint over fastened or welded joints, but also because of the flexibility to joint different materials. Other advantages include the smaller surface geometry disruption, more uniform stresses along the joint, ease of fabrication, design flexibility and corrosion prevention when bonding different materials [1]. In the automotive industry, this increases the design flexibility and gives better possibilities for optimization, resulting in weight reduction and more competitive vehicles. Klarbring [2] showed by an asymptotic analysis that the behaviour of thin adhesive layers between stiff adherends is ruled by two straining modes: elongation and shear (whose derivative variables are the normal, σ, and shear stresses, τ, respectively). Although this approach is a simplification of the rigorous stress state at the adhesive layer, many previous studies enable concluding that the simplification is accurate for reproducing the macro-behaviour of adhesive layers leading to the strength prediction of the bonded structures [3]. One justification for this, for ductile adhesives in particular, was given by Andersson and Stigh [4]: the damaged or Fracture Process Zone (FPZ) develops by a significant length beyond the crack tip, which makes the fracture toughness (G_C) of adhesives not particularly dependent on the precise details of stresses at the crack tip.

In any field of industry, the large-scale application of a given joint technique supposes that reliable tools for design and failure prediction are available. Analytical models, for which a comprehensive discussion and comparison is given

by Adams et al. [5], are limited for damage growth analysis. The concepts of Linear Elastic Fracture Mechanics (LEFM) can be used to analyse fracture of adhesive bonds [6], although involving a few limitations, the most relevant ones being (1) the assumed stress fields are not correctly captured when large-scale plasticity is present and (2) in most cases the purpose is to analyse undamaged joints, i.e., without any sort of macroscopic defect [7]. Thus, these conventional techniques are not the most applicable for bonded joints, unlike CZM, which assumes that the FPZ can be described at a macro-scale by a law relating the cohesive tractions (t_n for tension and t_s for shear) and the relative separations at the crack tip (δ_n for tension and δ_s for shear). By combining concepts such as the cohesive tractions and G_C of materials, it is straightforward to initiate damage in materials and enable its propagation. Whilst CZM principles date back to the works of Dugdale [8] and Barenblatt [9], it was only decades later that debonding under mixed-mode (i.e., tensile and shear combination) was addressed, e.g., in the work of Tvergaard and Hutchinson [10]. The cohesive laws are independently characterized for each loading mode and each transition in the global (mixed-mode) law is assessed by different criteria. Mode-mixicity is highly relevant for bonded joint failure analysis since, due to the complex loadings and crack growth between stronger adherends, cracks in adhesive joints mostly propagate under mixed-mode. This has led to the application of this technique to adhesively-bonded structures in the following years [11], in conjunction with development and testing of refined damage onset and failure criteria, different cohesive law shapes and improved cohesive law estimation techniques [3, 12]. Currently, a large variety of structural problems involving a wide range of mode-mixicities can be solved up to complete failure. The most important step in applying this technique is the estimation of the CZM law, although this is still not standardized [13]. A few data reduction techniques are currently available (the property identification technique, the direct method and the inverse method) that vary in complexity and expected accuracy. In all cases, pure fracture tests, such as the Double-Cantilever Beam (DCB) for mode I and the End-Notched Flexure (ENF) for mode II, are usually employed. Data reduction methods for the tensile fracture toughness (G_{IC}) by the DCB test are abundant, either conventional or not requiring crack length (a) measurements and accounting for plasticity [14]. This test specimen is also standardized (ASTM D3433-99 and BS 7991:2001). The ENF test geometry is less addressed, yet conventional and plasticity accounting methods are available [15].

The property identification method is based on building a parameterized CZM law by isolated materials properties. The main limitation is that the surrounding adherends lead to deviations between the bulk and thin adhesive bond cohesive properties, which are not accounted for [4]. The inverse method relies on a trial and error fitting analysis to experimental data, such as the load–displacement (P-δ) curve of fracture tests, allowing tuning of the simplified shape CZM laws for particular conditions [16]. Other grounds for comparison are the R-curve [17] or crack opening profile [18]. Direct methods output the cohesive law directly from experimental data. One of these consists of the direct tension or shear tests [19]. For the other, the cohesive law is obtained by measuring the J-integral and values of δ_n and δ_s [20], and differentiation of the tensile strain energy release rate (G_I)–δ_n or shear strain energy release rate (G_{II})–δ_s curves. The direct method is particularly attractive because it characterizes the adhesive under identical adherend restraining conditions to real applications and gives the exact shape of the CZM law. By this method, the full cohesive law is evaluated up to crack initiation. Actually, G_C gradually increases as the specimen is loaded and it attains a steady-state value when the crack begins to propagate. The onset of crack propagation corresponds, in the cohesive law, to the last phase of the law (zero stresses) [4]. This could be a limitation for materials exhibiting growing values of toughness with the advancing crack (e.g., fibrous composites because of fibre bridging). However, this method gives an unambiguous measurement of G_C for homogeneous materials such as adhesive layers [21]. Ouyang and Li [22] developed a general J-integral model/direct method for an adhesively-bonded ENF specimen with dissimilar adherends, which could be adapted to the standard ENF specimen, i.e., with identical adherends. Investigations showed that G_{IIC} is independent of the initial crack length (a_0). Moreover, the shape of the shear cohesive law highly affects the critical load, particularly for short values of a_0. In the work of Leffler et al. [21], the value of G_{IIC} and shear CZM law of an epoxy adhesive (DOW Betamate XW1044-3) were assessed experimentally by a J-integral methodology applied to the ENF specimen. The experimental procedure consisted of measuring δ_s by a digital camera attached to a microscope while recording the P-δ data. Results showed relatively consistent results for different values of adherend thickness (t_P), while two experimental conditions were compared: constant displacement rate and constant shear deformation rate. By comparing the resulting cohesive laws (obtained by differentiation of the G_{II}-δ_s laws), results showed virtually identical τ values, although the values of G_{IIC} were slightly different, on account of the varying shear deformation rates. An identical methodology was followed by Ji et al. [23] to assess the influence of the adhesive thickness (t_A) on the interfacial behaviour of bonded joints between composite plates, considering values between 0.1 and 0.8 mm. Results indicated that the interfacial shear strength increased with higher t_A values. The shape of the measured laws was also influenced by this parameter. The same authors [24] extended the previous study considering steel adherends. Zhu et al. [7] characterized the tensile (DCB) and shear (ENF) cohesive laws of steel/polyurea/steel specimens by the J-integral/differentiation approach to obtain the rate dependency of

these laws considering nominal strain rates between 0.003 and 3 s^{-1}. The required value of δ_s for the *J*-integral calculation was obtained by a Charged-Coupled Device (CCD) camera with a measurement accuracy of 2 μm. The shear CZM laws were highly nonlinear. Additionally, they were strain rate-dependent, which was explained by the interfacial behaviour. Carlberger and Stigh [25] studied, by the *J*-integral/direct method, the mode I and mode II cohesive behaviour of adhesive layers of the epoxy adhesive Dow Betamate® XW1044-3 as a function of t_A. The ENF testing protocol for mode II characterization relied on using a Linear Variable Differential Transformer (LVDT) mounted between rigid supports, one fixed to each adherend, to provide the real-time measurement of δ_s. G_{IIC} showed to be more influent than the shear cohesive strength (t_s^0) by varying the value of t_A. However, the G_{IIC} dependency with t_A was much smaller than G_{IC}, although revealing an increasing trend with t_A. In the work of Marzi et al. [26], identical conclusions were found, following the procedure of Carlberger and Stigh [25]. A slightly different approach, but yet within the framework of the *J*-integral, is postulated by Stigh et al. [27], in which the adherends can deform plastically. This enables the specimen size to be reduced, but it requires the additional measurement of rotations at three locations in the ENF specimens during thes tests.

This work evaluated the value of G_{IIC} of bonded joints for three adhesives with distinct ductility, including a novel high strength and ductile polyurethane adhesive for the automotive industry. The experimental work consisted of the shear fracture characterization of the bond by a conventional and the *J*-integral techniques. Additionally, by the *J*-integral technique, the precise shape of the cohesive laws is defined. For the *J*-integral, a digital image correlation method is used for the evaluation of δ_s during the test, coupled to a Matlab® subroutine for automatic extraction of this parameter.

Experimental Work

Materials

The aluminium alloy AA6082 T651 was selected because of its high tensile yield stress (σ_y), which prevents adherend plasticization during the tests, which would cancel the validity of the G_{IIC} results by plastic dissipations in the adherends. This is an aluminium alloy with high strength and ductility, as shown by the mechanical properties obtained in the work of Campilho et al. [28]: Young's modulus (E) of 70.07±0.83 GPa, σ_y of 261.67±7.65 MPa, tensile failure strength (σ_f) of 324.00±0.16 MPa and tensile failure strain (ε_f) of 21.70±4.24 %. To compare the behaviour of different adhesives and to evaluate the method's capability under different scenarios, either brittle/ductile failure or varying orders of magnitude in the measured quantities by the optical method, the following adhesives were used: the brittle epoxy Araldite® AV138, the ductile epoxy Araldite® 2015 and the ductile polyurethane Sikaforce® 7752. A comprehensive mechanical and fracture characterization of these adhesives was recently undertaken in different studies by the authors [3, 20, 28, 29]. Bulk specimens loaded in tension enabled obtaining E, σ_y, σ_f and ε_f. The values of G_{IC} and G_{IIC} were obtained by conventional data reduction schemes using the DCB and ENF tests, respectively. Table 1 presents the relevant mechanical and fracture data of the adhesives.

Joint Geometries, Fabrication and Testing

Figure 1 shows the characteristic geometry and dimensions of the ENF joints: mid-span L=100 mm, a_0≈60 mm, t_P=3 mm, width b=25 mm and t_A=0.2 mm. The joints were assembled under controlled conditions of temperature and humidity. Before bonding, the adherends' faces to join were roughened by grit blasting followed by cleaning with acetone. Curing was carried out in a steel mould to assure the correct alignment between adherends and also the position of the calibrated spacers. Actually, calibrated steel spacers were inserted between the adherends at both edges of the adhesive layer to obtain a constant value of t_A in the adhesive bond, after applying demoulding agent to enable removal after curing. The crack tip spacer, which aims at producing a sharp pre-crack in the adhesive layer to ensure stable crack growth at the beginning of crack propagation, was composed of a 0.1 mm thick razor blade between calibrated steel spacers. These were stacked and glued together (Fig. 2(a)), making a total thickness of 0.2 mm. The cutting edge of the blade was offset from the sheets and positioned facing the adhesive layer before application of the adhesive such that, after curing of the adhesive, a sharp pre-crack was produced at the adhesive layer's edge (Fig. 2(b)). The spacer at the opposite edge of the crack has the sole purpose of assuring the selected t_A value and, thus, it is only composed of a 0.2 mm thick component. Application of demoulding agent to the spacers enabled their extraction after curing of the adhesive. Curing was performed at room temperature. Final set-up of the specimens was then undertaken with the removal of the steel spacers and painting the crack tip path with brittle white paint to better visualize a during the tests. After this procedure, the crack was manually propagated for few millimetres to fully guarantee a stable initiation of crack growth and a black numbered scale was glued in both upper and lower adherends to aid the parameter extraction for the direct method. For optimization of the optical data acquisition process, the scales were positioned such that the manually-propagated crack tip was exactly at the mark of 10 mm in the scale. Figure 3 shows a specimen after this procedure, in which the crack tip spacer induced a pre-crack approximately at the 7 mm mark in the scale, with the manual propagation extending it up to the mark of 10 mm. The tests

Table 1 Properties of the adhesives Araldite® AV138, Araldite® 2015 and Sikaforce® 7752 [3, 20, 28, 29]

Property	AV138	2015	7752
Young's modulus, E [GPa]	4.89±0.81	1.85±0.21	0.49±0.09
Poisson's ratio, ν	0.35 [a]	0.33 [a]	0.30 [a]
Tensile yield strength, σ_y [MPa]	36.49±2.47	12.63±0.61	3.24±0.48
Tensile failure strength, σ_f [MPa]	39.45±3.18	21.63±1.61	11.48±0.25
Tensile failure strain, ε_f [%]	1.21±0.10	4.77±0.15	19.18±1.40
Shear modulus, G [GPa]	1.56±0.01	0.56±0.21	0.19±0.01
Shear yield strength, τ_y [MPa]	25.1±0.33	14.6±1.3	5.16±1.14
Shear failure strength, τ_f [MPa]	30.2±0.40	17.9±1.8	10.17±0.64
Shear failure strain, γ_f [%]	7.8±0.7	43.9±3.4	54.82±6.38
Toughness in tension, G_{IC} [N/mm]	0.20 [b]	0.43±0.02	2.36±0.17
Toughness in shear, G_{IIC} [N/mm]	0.38 [b]	4.70±0.34	5.41±0.47

[a] manufacturer's data

[b] estimated in reference [28]

comprised a total of twenty-four specimens (eight for each adhesive) and they were carried out at room temperature in a Shimadzu AG-X 100 testing machine equipped with a 100 kN load cell. For the required test documentation, an 18 MPixel digital camera was used, with no zoom and fixed focal distance to approximately 100 mm, to obtain high resolution images for further application of the previously discussed techniques. The test setup is depicted in Fig. 4. This procedure made possible obtaining a during the test by a manual measurement method, necessary to measure G_{IIC} by the conventional and J-integral techniques. The manual measurement was undertaken by the individual analysis of each image and comparison against the scale marks using zooming tools. With the reported camera resolution, the average pixel size was approximately 0.011 mm, enabling high precision measurements. Only one conventional method does not require measurement of a, as it will be detailed further in this work. Moreover, this procedure also enables estimating δ_s by a developed Matlab® algorithm, necessary for the application of the direct method. The correlation of the mentioned parameters with the P-δ data was done by the time elapsed since the beginning of each test.

Methods to Determine G_{IIC}

Data reductions schemes that are based on LEFM principles and without accounting for the adhesives' ductility usually underestimate G_{IIC} [15]. In this work, apart from the J-integral, the following conventional techniques were tested: Compliance Calibration Method (CCM), Direct Beam Theory (DBT), Corrected Beam Theory (CBT) and Compliance-Based Beam Method (CBBM).

Conventional Methods

The classical data reduction schemes to obtain G_{IIC} are usually based on compliance calibration or beam theories. The CCM is based on the Irwin-Kies equation [30]

$$G_{IIC} = \frac{P^2}{2b}\frac{dC}{da}, \quad (1)$$

where $C=\delta/P$ is the specimen's compliance. Cubic polynomials ($C=C_1a^3+C_0$) were used to fit the $C=f(a)$ curves, resulting into

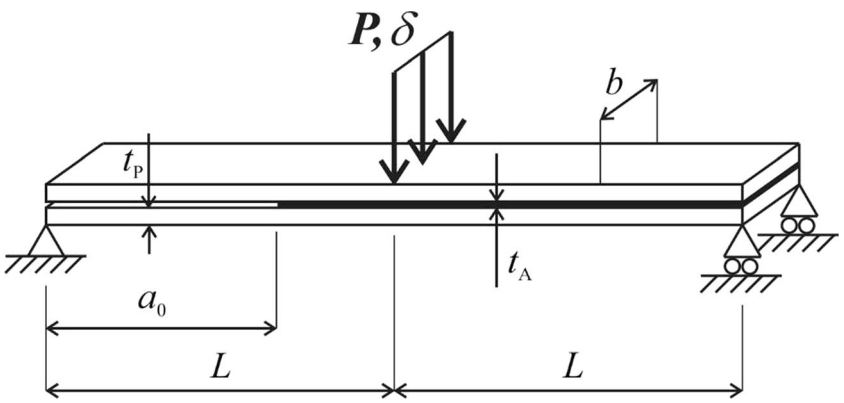

Fig. 1 Geometry of the ENF specimens

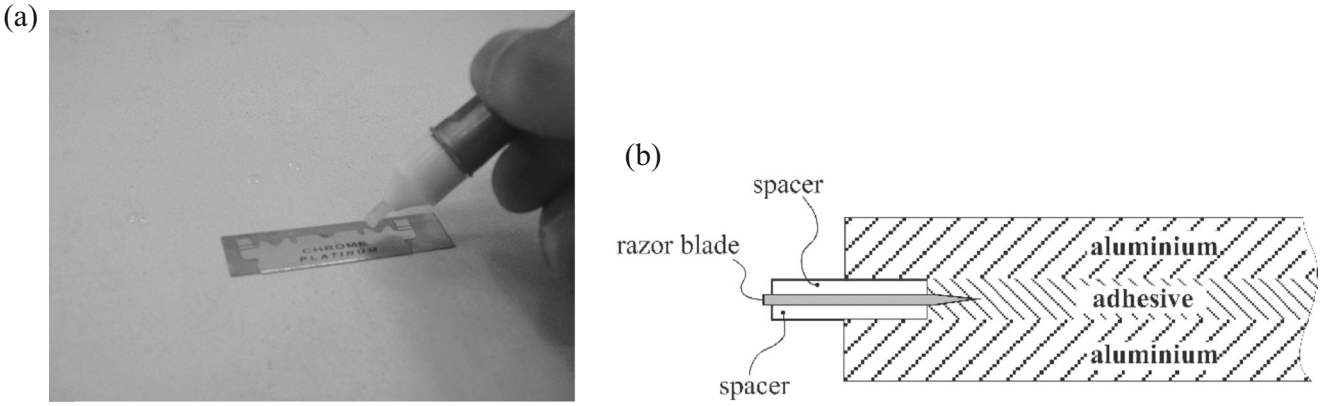

Fig. 2 Gluing of crack tip spacer (**a**) and schematics of the crack tip spacer (**a**)

$$G_{\mathrm{IIC}} = \frac{3P^2C_1a^2}{2b}. \tag{2}$$

Beam theories were also used to measure G_{IIC}. The DBT, which does not account for crack length corrections to consider the effects of shear deformation (unlike the CBT), is given as [31]

$$G_{\mathrm{IIC}} = \frac{9P\delta a^2}{2b\left(2L^3 + 3a^3\right)}. \tag{3}$$

The CBT was proposed by Wang and Williams [32] and is written as

$$G_{\mathrm{IIC}} = \frac{9(a + 0.42\Delta_{\mathrm{I}})^2P^2}{16b^2E_{\mathrm{x}}{t_{\mathrm{P}}}^3}, \tag{4}$$

where E_{x} is the adherends, E value in the length direction and Δ_{I} is a crack length correction to account for shear deformation [15]

$$\Delta_{\mathrm{I}} = t_{\mathrm{P}}\sqrt{\frac{E_{\mathrm{x}}}{11G_{\mathrm{xy}}}\left[3{-}2\left(\frac{\Gamma}{1+\Gamma}\right)^2\right]}, \tag{5}$$

in which G_{xy} is the in-plane shear modulus and Γ is given by

$$\Gamma = 1.18\sqrt{\frac{E_{\mathrm{x}}E_{\mathrm{y}}}{G_{\mathrm{xy}}}}, \tag{6}$$

where E_{y} is the value of E of the adherends in the thickness direction. The CBBM was also developed for the ENF specimen [15], enabling the estimation of G_{IIC} only using the experimental compliance. This technique relies on an equivalent crack that does not require measurement and is computed based on the current specimen's compliance. The equivalent crack length, a_{eq}, is introduced, which accounts for the FPZ effects at the crack tip (not taken into account when the real value of a is considered). G_{IIC} can be obtained by the following expression

$$G_{\mathrm{IIC}} = \frac{9P^2{a_{\mathrm{eq}}}^2}{16b^2E_{\mathrm{f}}{t_{\mathrm{P}}}^3}. \tag{7}$$

Detailed explanations of the method can be found in reference [15]. E_{f} is an equivalent flexural modulus obtained from the specimen's initial compliance and value of a_0.

J-integral Method

This Section describes the direct method for G_{IIC} and cohesive law estimation by ENF experiments [7, 21, 25]. This technique relies on the simultaneous measurement of the *J*-integral and δ_{s} (Fig. 5). As previously discussed [20], the *J*-integral is suited to the non-linear elastic behaviour of materials, but it remains applicable for plastic monotonic loadings, as it is the case of the ENF test protocol. The proposed G_{II} evaluation expression results from using alternate integration paths to extract the *J*-integral [33], resulting in the following closed-form expression for G_{II} [21]:

$$G_{\mathrm{II}} = \frac{9}{16}\frac{\left(P_{\mathrm{u}}a\right)^2}{E_{\mathrm{x}}{t_{\mathrm{P}}}^3} + \frac{3}{8}\frac{P_{\mathrm{u}}\delta_{\mathrm{s}}}{t_{\mathrm{P}}}, \tag{8}$$

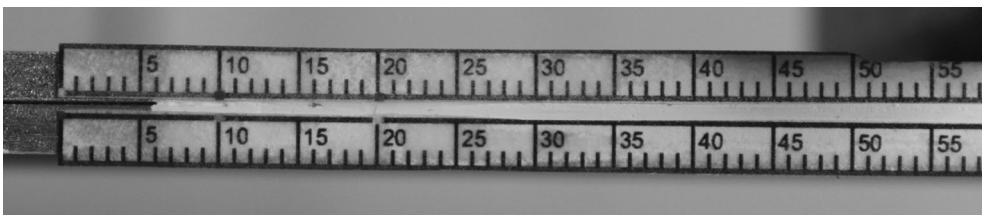

Fig. 3 Side view of a specimen prepared for testing

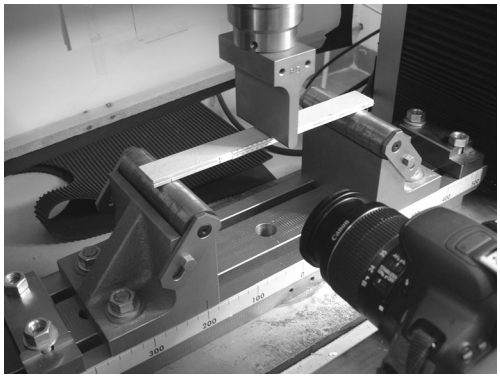

Fig. 4 ENF test setup with a specimen ready for testing

where P_u is the current load per unit width at the loading cylinder. The first term corresponds to the LEFM solution. The second term relates to the influence of a flexible adhesive layer, and it can give a large contribution to G_{II} [21]. The accuracy of this expression requires the linear elastic behaviour of the adherends, which needs to be checked during the design of the specimens' geometry and verified after each test is done. By evaluating the *J*-integral around the damage region or FPZ of the adhesive layer, it is possible to write

$$G_{II} = \int_0^{\delta_{sc}} t_s(\delta_s)\mathrm{d}\delta_s. \tag{9}$$

δ_{sc} is the shear crack-tip end-opening at failure of the cohesive law. Expression (9) gives a direct relation between the stress state at the crack tip and G_{II}. The evolution of G_{II} with δ_s is as follows: before crack propagation, G_{II} increases up to attaining G_{IIC}. At this stage, the crack begins to propagate. G_{IIC} is thus obtained by the steady-state value of G_{II} in the G_{II}-δ_s plot. This point in the plot corresponds to cancelling of the corresponding stress component and consequent formation of a crack. The $t_s(\delta_s)$ plot or shear cohesive law of the adhesive layer is thus estimated by fitting of the resulting G_{II}-δ_s curve and differentiation with respect to δ_s [21]

$$t_s(\delta_s) = \frac{\partial G_{II}}{\partial \delta_s}. \tag{10}$$

Differentiation can be performed by polynomial functions or least square adaptions of Prony-series to the G_{II} data, this last technique to be recommended when the polynomial expressions reveal to be rough approximations of the experimental data [25]. Because of compression and friction effects at the crack faces of the ENF specimen eventually compromising the cohesive law accuracy, some authors [7] considered instead the Arcan test method to obtain the shear cohesive law of adhesive layers.

Optical algorithm for parameter extraction – ENF specimen

A numerical algorithm was developed to measure δ_s based on image processing and tracking of a set of reference points throughout a sequence of images. The optical method requires the identification of 6 points, from p_1 to p_6 (Fig. 6), which define the curvatures of the top and bottom adherends. δ_s is given by the arc length between p_3' and p_4', which are the projections of p_3 and p_4 into the medial curve of the specimen. The process starts by manually identifying the 6 points in the first picture of a test. Points p_1 to p_6 are printed with a distinct colour, which helps finding their correct locations. Starting from the points in the first picture, the points of the following pictures are automatically tracked with an algorithm in Matlab®. Full details of the point tracking algorithm are presented in a previous work [20]. With this procedure, all 6 points locations are easily found for all pictures taken during an ENF test. On the other hand, the procedure to measure δ_s is described next in detail since it was specifically tuned for this parameter and test method (ENF test) with all its specificities.

Compared to the commercially available Digital Image Correlation (DIC) systems, the advantages of using the

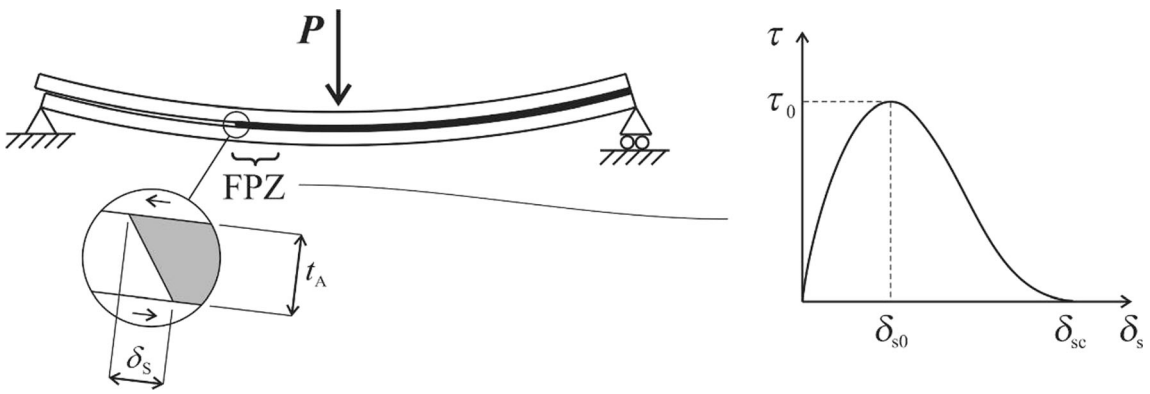

Fig. 5 ENF specimen under loading, with description of the analysis parameters

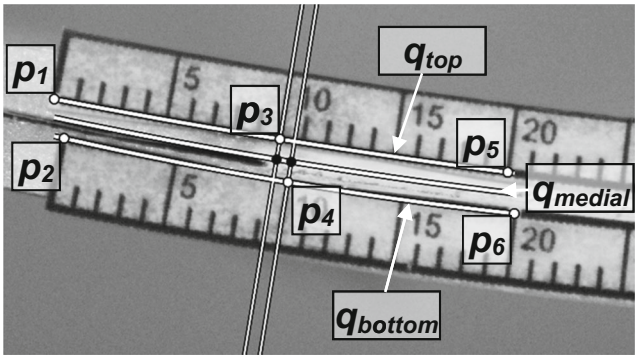

Fig. 6 Illustration of the points taken by the optical method (p_1 to p_6), the curves fitted to those points (q_{top} and q_{bottom}) and the medial curve (q_{medial}) where δ_s is measured

proposed method are the lower equipment costs (only a camera with large resolution is necessary), and the higher resolution of the camera (20 MPixel or more compared to 2 to 5 MPixel of the commercially available systems).

Computation of δ_s The value of δ_s is obtained by measuring the arc length between p_3 and p_4 on the curve that lies between the two adherends, the medial curve. The curvatures of the adherends are described by quadratic polynomials

$$q_i(x) = a_i x^2 + b_i x + c_i, \tag{11}$$

where q_i represents the curvature of adherend i, and a_i, b_i and c_i are the coefficients of the polynomial. The coefficients are found by fitting the quadratic functions to the y coordinates of the points in the least squares sense, such as $q_{top}([x_1,x_3,x_5]^T)=[y_1,y_3,y_5]^T$ and $q_{bottom}([x_2,x_4,x_6]^T)=[y_2,y_4,y_6]^T$. In theory, q_{top} and q_{bottom} would be strictly parallel and δ_s could be calculated by projecting p_3 to the bottom curve, or p_4 to the top curve. However, in practise, this is not verified and, thus, δ_s is calculated by the projections of p_3 and p_4 into the medial curve of the specimen. The medial curve, q_{medial}, is defined by averaging the coefficients of the bottom and top curvatures,

$$\begin{aligned} q_{medial}(x) &= a_{medial}x^2 + b_{medial}x + c_{medial} \\ &= \frac{a_{top}+a_{bottom}}{2}x^2 + \frac{b_{top}+b_{bottom}}{2}x \\ &\quad + \frac{c_{top}+c_{bottom}}{2}. \end{aligned} \tag{12}$$

The projection of a point $p_i=(x_i,y_i)$ into the medial curve is obtained by finding the line that is perpendicular to the medial curve and that passes by p_i. The perpendicular to the medial curve at a given point is the line that is perpendicular to the tangent of the curve at that point, which is given by the first derivative of q_{medial},

$$q'_{medial}(x) = 2a_{medial}x + b_{medial}. \tag{13}$$

The projection (x_i',y_i') of a given point (x_i,y_i) is found by solving the system

$$\begin{cases} a_{normal} = -\dfrac{1}{2a_{medial}x_i' + b_{medial}} \\ b_{normal} = y_i' - a_{normal}x_i' \\ y_i = a_{normal}x_i + b_{normal} \\ y_i' = a_{medial}x_i'^2 + b_{medial}x_i' + c_{medial} \end{cases}, \tag{14}$$

where the first two equations define the coefficients a_{normal} and b_{normal} of the line that is perpendicular to q_{medial} and that passes by the projected point (x_i',y_i'), the third equation forces the perpendicular to pass by the original point (x_i,y_i), and the forth equation forces the projected point to belong to the medial curve. This non-linear system of equations is numerically solved with the Matlab®'s *vpasolve* function, and always returns a single solution in the real numbers domain. Having p_3' and p_4', δ_s^p (the value of δ_s in pixels) may be found by measuring the arc length of q_{medial} between these two points,

$$\delta_s^p = \int_{x_3'}^{x_4'} \sqrt{1+\left(\frac{dy}{dx}\right)^2}dx = \int_{x_3'}^{x_4'} \sqrt{1+(a_{medial}x+b_{medial})^2}dx. \tag{15}$$

δ_s^p is in image units (pixels) and needs to be converted to real world units (e.g., millimeters). Since the length of the arcs (p_1, p_5) and (p_2, p_6) is known to be d=20 mm, this is used to find the pixel size and, thus, convert δ_s^p to millimeters,

$$\delta_s^t = \frac{\delta_s^p d}{2}\left(\int_{x_1}^{x_5}\sqrt{1+(a_{top}x+b_{top})^2}dx + \int_{x_2}^{x_6}\sqrt{1+(a_{bottom}x+b_{bottom})^2}dx\right)^{-1}. \tag{16}$$

The pixel size was on average 0.011 mm and, thus, the estimated maximum error of the image acquisition process is ±0.006 mm. Finally, δ_s can be defined as

$$\delta_s = \delta_s^t - \delta_s^0 \tag{17}$$

where δ_s^0 is the initial value of δ_s^t.

Results

The ENF specimens were tested following the previously described procedure. All specimens revealed cohesive failure of the adhesive layer for the full extension of the crack, while the adherends behaved elastically. This is mandatory for the correct calculation of G_{IIC} and shear cohesive law of the adhesive layer.

G_{IIC} Calculation by the Conventional Methods

The G_{IIC} values were estimated by the data reduction methods mentioned in the Section "Conventional Methods". The

experimental P-δ curves for each adhesive system revealed a good agreement between specimens. Figure 7 gives the comparison of the P-δ curves for the adhesive Sikaforce® 7752 (δ corresponds to the loading point displacement). The P-δ curves were truncated at the region of crack attaining the proximity of the loading cylinder, because here the G_{II} measurements lose validity. The CCM requires calculating dC/da during the test and this is a very critical step, because of the large effect on the outcome of the R-curve [15]. Figure 8 shows, as an example, the C=f(a) curve and 2nd degree polynomial approximation for a specimen bonded with Araldite® 2015. The R-curves, which relate G_{II} vs. a, are shown in Fig. 9 (considering one specimen for each adhesive type). As it can be observed in Fig. 9(c), only the CBBM data reduction method was equated for the adhesive Sikaforce® 7752. Actually, for this particular adhesive, and due to its ductility, the brittle layer of white paint cracks before real crack growth, which prevented the application of the other methods. For all adhesive systems and data reduction techniques, the R-curve is consistent with the theoretically steady-state value of G_{II} that should be obtained throughout the crack growth phase, although with minor oscillations that are natural in experimental data. On the other hand, this steady-state behaviour should only span from the crack growth onset up to the vicinity of the loading (i.e., middle) cylinder. At this point, the compression effects by this cylinder on the crack tip obstruct crack growth, thus artificially increasing the measured value of G_{II}. The steady-state value of G_{II} gives a measurement of G_{IIC} [34]. Another distinctive feature that is patent in Fig. 9 is the deviation to the right of the CBBM curves of the adhesives Araldite® AV138 and 2015 relatively to the techniques requiring a measurement, which is justified by the inclusion of the FPZ in a_{eq}, thus rendering the real crack lengthier than the measured one [15]. The values of a_0 for the specimens of Fig. 9 are 69.31 mm (Araldite® AV138), 59.67 mm (Araldite® 2015) and 49.92 mm (Sikaforce® 7752). These quantities agree with the vertical increase of G_{II} in the G_{II}-a curves for the

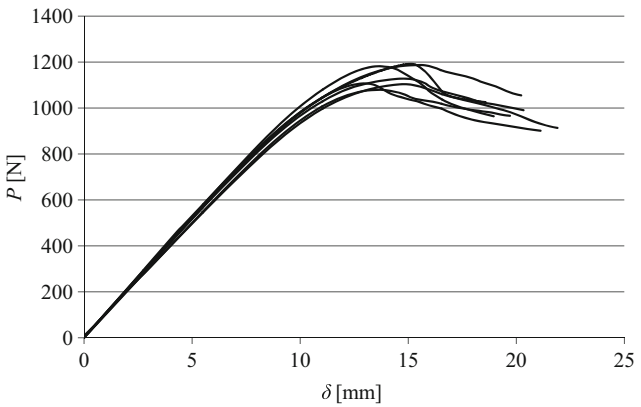

Fig. 7 Experimental ENF test P-δ curves for the adhesive Sikaforce® 7752

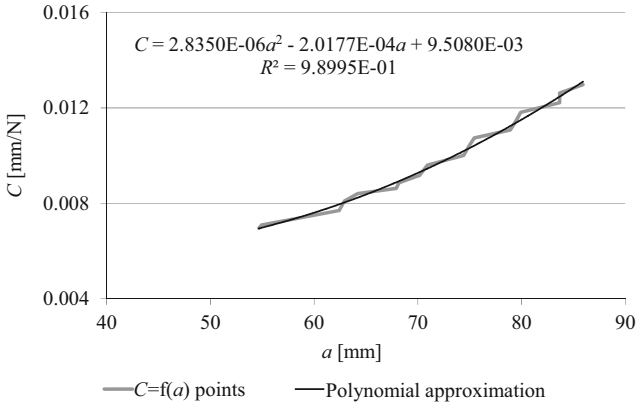

Fig. 8 Example of C=f(a) curve for a specimen bonded with the adhesive Araldite® 2015 and polynomial approximation

techniques requiring measurement of a (CCM, DBT and CBT). On the other hand, the corresponding a_{eq} values are 74.13 mm, 69.66 mm and 74.40 mm (by the same order), due to the consideration of the plastic zone. By comparing the initial values of a_{eq} with a_0, an increasing difference is found with the adhesive ductility, which can also be observed in the R-curves of the Araldite® AV138 and 2015 in Fig. 9 (comparing the onset of the R-curves for the conventional methods). By comparing the curves for the adhesives Araldite® AV138 and 2015 by the different methods, the CBT clearly under predicts the CCM, DBT and CBBM. Table 2 summarizes the values of G_{IIC} (N/mm) of all specimens, considering the average G_{II} value during the steady-state portion of the curve, and respective average values and deviation for each adhesive and data reduction technique. From the complete set of tested specimens, few of these were not valid. Furthermore, for some specimens (marked with [a]) the CCM analysis was rendered unpractical because of difficulties in obtaining dC/da. Between specimens of the same adhesive and method, results agree quite well. Actually, for each set adhesive/data reduction method, the standard deviation is typically below 10 % of the G_{IIC} average values. Additionally, for each adhesive system, the results between data reduction methods were consistent, except for the CBT. Considering the CBBM values as reference, the CBT under predicts these values by 17.7 % (Araldite® AV138) and 17.0 % (Araldite® 2015).

G_{IIC} and CZM Law Calculation by the J-integral

The results presented here follow the direct method procedure depicted in the Section "J-integral Method" for the shear cohesive law estimation of bonded joints. Initially, the value of δ_s was obtained with 5 s intervals for each test specimen, following the automatic data extraction procedure described in the Section "Optical algorithm for parameter extraction – ENF specimen". Figure 10 gives a representative example of the

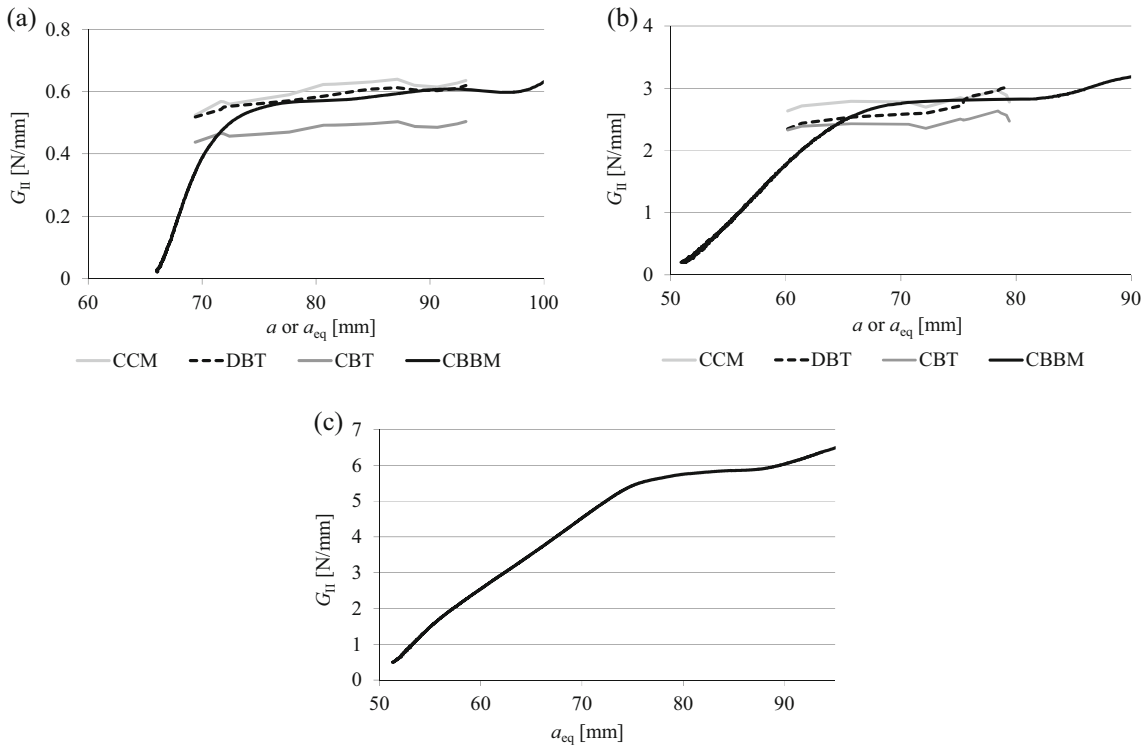

Fig. 9 Comparison of representative *R*-curves for each of the adhesives: (**a**) Araldite® AV138, (**b**) Araldite® 2015 and (**c**) Sikaforce® 7752

variation of δ_s with the time elapsed since the beginning of the test for each one of the tested adhesives. The raw curves from the point tracking algorithm and the adjusted polynomial laws, attained by making δ_s(testing time=0)=0, are presented in this figure. The curves were truncated at crack initiation since, from this point on, the data is no longer relevant for the direct method. It should be mentioned that, depending on the specimen under analysis, different degree polynomials were selected in order to attain the best correlation factor, *R* (which is also valid for the polynomial to fit the G_{II}-δ_s law, to be discussed further in this Section). While the polynomial approximation is necessary to remove the noise from the raw curve, the mentioned procedure to obtain the adjusted polynomial laws was required on account of eventual initial offsets while preparing the specimens that made the δ_s value not to be nil at the beginning of each test. The evolution of δ_s in Fig. 10 is exponential with the testing time, and this is consistent with previous works. Leffler et al. [21] obtained an exponentially increasing evolution of the shear deformation rate of the ENF tests by using an extensometer attached to the both adherends at the crack tip. Between adhesives, a clear difference can be found in the maximum δ_s values, which closely follow the adhesive ductility. Inclusively, δ_s at crack initiation for the

Table 2 Values of G_{IIC} [N/mm] for the three adhesives obtained by all methods

Adhesive	Araldite® AV138				Araldite® 2015				Sikaforce® 7752
Specimen	CCM	DBT	CBT	CBBM	CCM	DBT	CBT	CBBM	CBBM
1	0.469	0.566	0.440	0.572	3.029	3.083	2.644	3.420	5.825
2	[a]	0.709	0.566	0.712	–	–	–	–	5.877
3	[a]	0.650	0.608	0.724	3.675	2.401	2.177	2.545	5.474
4	–	–	–	–	3.214	2.916	2.544	2.943	4.813
5	[a]	0.578	0.519	0.594	2.812	2.741	2.476	2.801	5.676
6	0.568	0.579	0.487	0.562	3.357	3.088	2.644	3.136	5.648
7	0.605	0.581	0.478	0.576	2.696	2.831	2.624	2.901	5.619
8	0.603	0.583	0.481	0.585	3.008	2.952	2.512	3.025	–
Average	0.561	0.606	0.511	0.618	3.113	2.859	2.517	2.967	5.562
Deviation	0.064	0.053	0.058	0.069	0.334	0.238	0.164	0.273	0.356

[a] Polynomial fitting difficulties

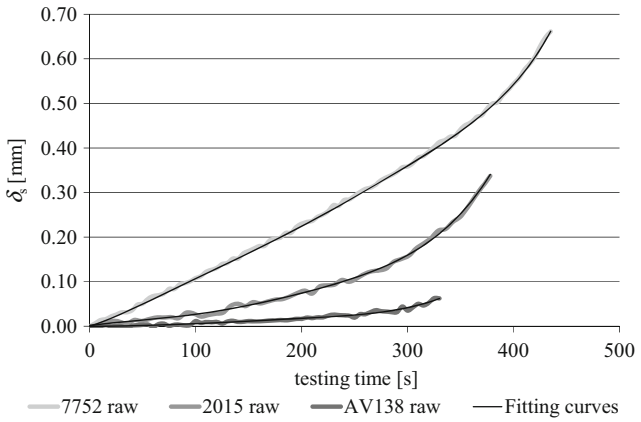

Fig. 10 Plot of δ_s – testing time for a specimen of each tested adhesive: raw curve and polynomial approximations

Araldite® AV138 is under 1/10 of a millimetre. After having the δ_s-testing time plots, it was possible to estimate the G_{II}-δ_s relationship by direct application of equation (8). The G_{IIC} estimate is given by the steady-state value of G_{II} in the G_{II}-δ_s curve, which corresponds to the onset of crack propagation [25]. Figure 11 shows the G_{II}-δ_s curve for the same specimens of Fig. 10 and the selected polynomial approximations (the Araldite® AV138 curve is in secondary axis for clarity). The shape of these curves is consistent with published data in the literature [20, 35]. It can be found that, at the beginning of the test, G_{II} increases very slowly, but the rate of improvement quickly increases and ultimately a steady-state value is attained. As previously mentioned, this last stage indicates the onset of crack growth and gives the G_{IIC} estimate. A clear difference is observed between the three adhesives regarding the range of G_{II} values up to attaining the steady-state value corresponding to G_{IIC}. Moreover, the horizontal span of the curves also shows the difference in δ_s previously discussed in Fig. 10. For the specimens depicted in the figures, the measured values of G_{IIC} [N/mm] are 0.479 (Araldite® AV138), 3.444 (Araldite® 2015) and 5.790 (Sikaforce® 7752). The overall G_{IIC} results for all specimens

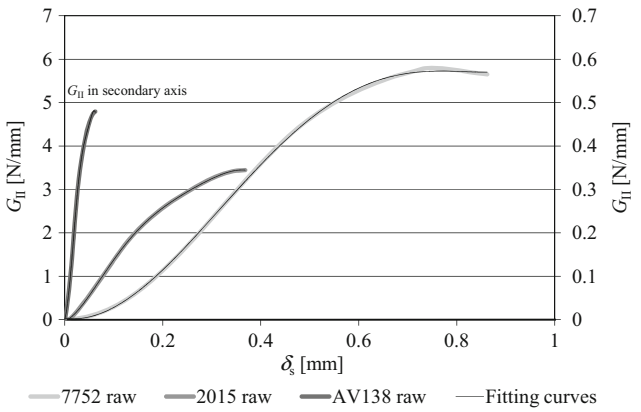

Fig. 11 Plot of G_{II} – δ_s for a specimen of each tested adhesive: raw curve and polynomial approximations

are presented in Table 3. These reveal a good repeatability, with percentile deviations under 10 %, except for the Araldite® AV138. The results are consistent with the CBBM of Table 2, with a maximum deviation between average values of 7.21 % for the Araldite® 2015.

It is also relevant to perform a comparison between the data of Tables 2 and 3, and the G_{IIC} values of these adhesives predicted in previous works (Table 1). For the Araldite® AV138, the average G_{IIC} presented in this work by the *J*-integral is 52.6 % higher than that of Table 1. The data of Table 1 refers to a previous work [28] in which the values of G_{IC} and G_{IIC} were determined by an inverse fitting method (i.e., G_{IIC} was not directly measured, but fitted to a given joint geometry). Thus, the procedure undertaken in the present work is clearly more robust. In the case of the Araldite® 2015, the data of Table 1 corresponds to using conventional G_{IIC} data reduction methods by ENF specimens with higher stiffness (carbon-epoxy composite) than the aluminium used in the present work. Previous works [36] showed that G_{IC} increases with the adherends' stiffness because of the larger dimensions of the FPZ ahead of the crack tip. In the authors' opinion, this is also valid for G_{IIC} and is on the basis of the 32.3 % reduction found in G_{IIC} in this work by the *J*-integral. The G_{IIC} values for the Sikaforce® 7752 in Table 1 pertain to the same experimental ENF tests, although processed in a previous work [29]. The small difference between the data of Table 1 and Table 2/Table 3 is due to data processing being performed by different individuals. A positive difference of 4.8 % was found in this work by the *J*-integral, compared to the data of Table 1.

To apply the differentiation procedure represented by equation (10) and estimate the shear CZM laws, polynomial functions were applied to the raw G_{II}-δ_s data of each specimen. Generally, it was possible to achieve a high degree of accuracy between 4th and 6th degree functions (R varied between 0.96 and 0.99). Figure 12 shows the full set of t_s-δ_s curves obtained by the direct method for the three adhesives. The curves show

Table 3 Values of G_{IIC} [N/mm] for the three adhesives obtained by the *J*-integral

Specimen	Araldite® AV138	Araldite® 2015	Sikaforce® 7752
1	0.552	3.444	–
2	0.732	3.585	5.067
3	0.676	2.873	6.050
4	–	3.298	5.360
5	0.566	3.123	6.070
6	0.533	3.140	5.173
7	0.523	3.080	5.790
8	0.479	2.901	6.160
Average	0.580	3.181	5.667
Deviation	0.090	0.249	0.459

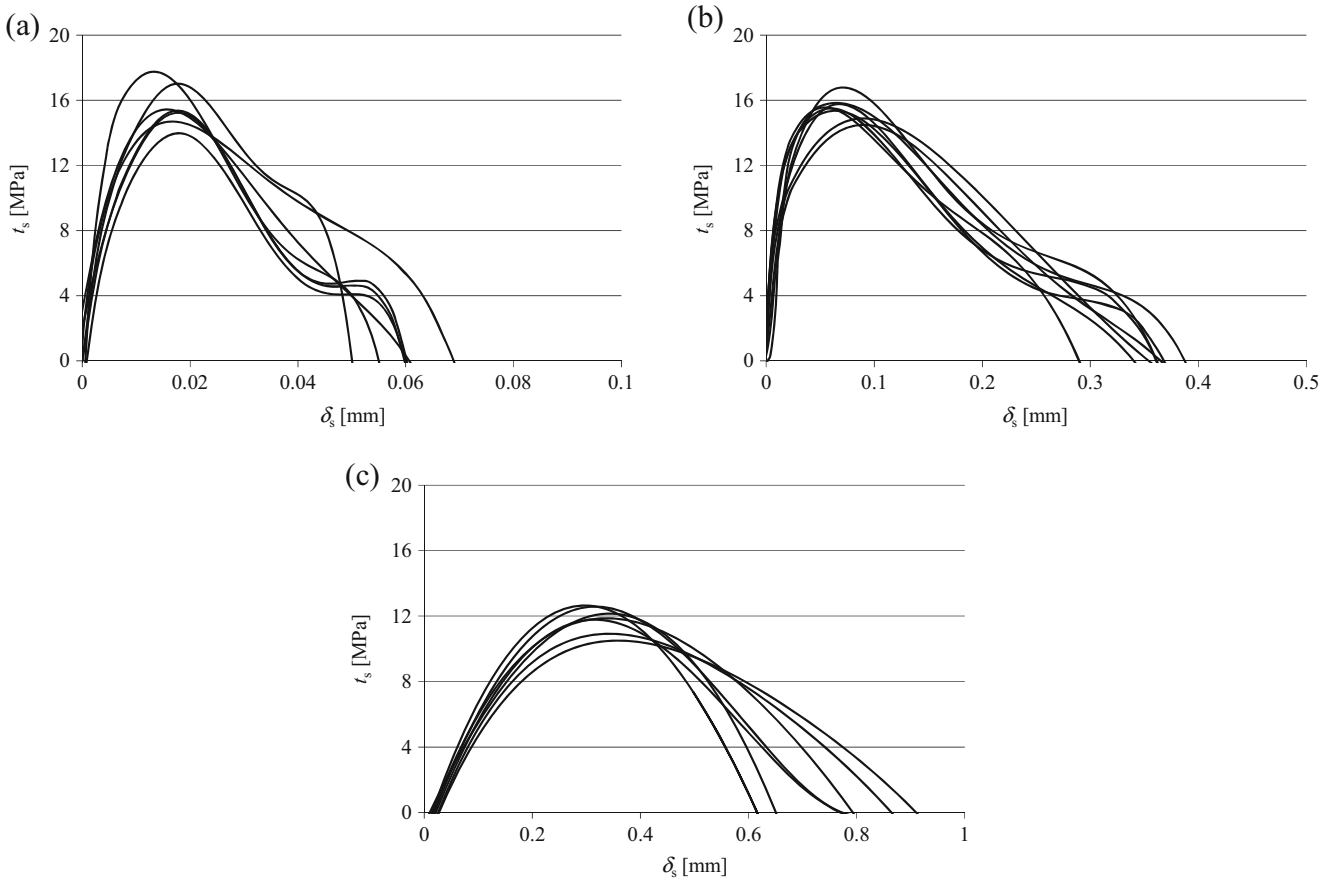

Fig. 12 Comparison of the full set of t_s-δ_s curves for each of the adhesives: (**a**) Araldite® AV138, (**b**) Araldite® 2015 and (**c**) Sikaforce® 7752

identical t_s^0 values between the Araldite® AV138 and 2015, while the Sikaforce® 7752 gives smaller values. The value of δ_{sc} also differs in accordance with the previously mentioned difference discussed for Fig. 10. For all adhesives, a good agreement was found between curves regarding the initial stiffness of the curves, t_s^0, descending part of the curves and δ_{sc}. The average and deviation of the cohesive parameters (with percentile deviation in parenthesis) were as follows. Araldite® AV138: t_s^0=15.6±1.39 MPa (8.9 %), δ_s^0=0.0167 ±0.00163 mm (9.80 %) and δ_{sc}=0.0618±0.0214 mm (34.6 %), Araldite® 2015: t_s^0=15.5±0.683 MPa (4.4 %), δ_s^0=0.0702±0.0122 mm (17.4 %) and δ_{sc}=0.372± 0.0246 mm (6.6 %) and Sikaforce® 7752: t_s^0=11.8± 0.807 MPa (6.9 %), δ_s^0=0.328±0.0182 mm (5.5 %) and δ_{sc}=0.781±0.107 mm (13.7 %). It can be considered that the scatter between specimens of the same adhesive is acceptable and shows a high correlation between specimens. The percentile deviation was generally under 10 %, except a few cases in which δ_s^0 or δ_{sc} exceeded this value. Figure 13 compares typical CZM laws for each adhesive and the parametrized CZM law that fits best each raw curve, either triangular or trapezoidal. The brittle Araldite® AV138 is best modelled by a triangular CZM law, while the other two adhesives are represented with more accuracy with a trapezoidal CZM law. However, the Araldite® 2015 could be modelled with a triangular CZM law as well with some level of accuracy to the raw curve. The obtained CZM laws pertain to the cohesive behaviour of the adhesive layer, thus clearly reflecting the adhesives' ductility. In the presence of interfacial rather than cohesive failures, these are usually brittle because a lack of adhesion occurs before the adhesive's ductility is fully exploited

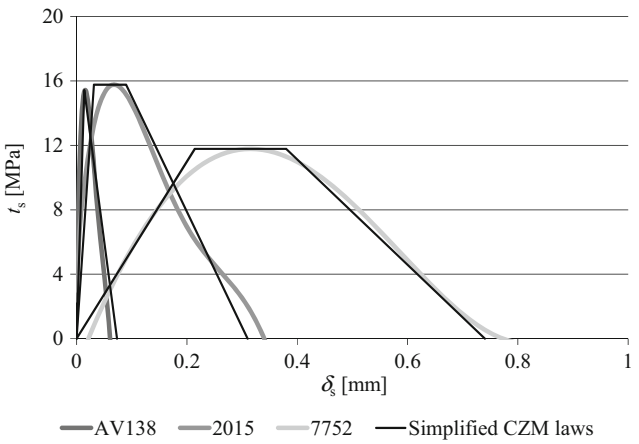

Fig. 13 Comparison of representative t_s-δ_s curves for each of the adhesives with simplified CZM laws

[37]. Thus, predicted CZM laws without plastic behaviour are expected. Moreover, the *J*-integral approach undertaken in this work is continuum-based, i.e., it characterized the cohesive behaviour of the adhesive as a whole. Thus, it is expected that the CZM laws are t_A and rate dependent [38] and that accurate results in the strength prediction of generic joints are only obtained in the presence of a similar t_A value and if quasi-static loading conditions are met. The results of Fig. 13 can also be compared with the analysis of Constante et al. [39] relating to the tensile CZM law estimation by the direct method considering the Araldite® AV138 and 2015, and a polyurethane with similar characteristics to the Sikaforce® 7752 (the Sikaforce® 7888). In fact, under tension, the Araldite® AV138 also reveals to be extremely brittle and a triangular law was proposed, while the ductility of the Araldite® 2015 and Sikaforce® 7888 could be reproduced by a trapezoidal CZM law.

Identically to G_{IIC}, the obtained values of t_s^0 patent in Figs. 12 and 13 can also be compared to the data of Table 1. By evaluating the previously mentioned average values by the direct method against the shear failure strength (τ_f) of Table 1, differences of −48.3 %, −13.4 % and +16.0 % were found for the Araldite® AV138, Araldite® 2015 and Sikaforce® 7752, respectively. This deviation between t_s^0 and τ_f can be explained in light of the difference between a local quantity (cohesive strength at the crack tip) and the overall response of a bulk material, respectively. Actually, at the crack tip, the strain constraining effects imposed by the adherends and the typical mixed-mode crack propagation (oppositely to crack growth orthogonally to the direction of maximum principal stress in bulk materials), often lead to non-negligible variations between these two quantities [15].

Results Comparison with Another *J*-integral Technique

A nonlinear *J*-integral solution applied to the ENF specimen is available in the work of Ouyang and Li [22] for G_{II} and CZM law estimation, generically developed for ENF specimens with different adherends. A comparison is made regarding this formulation and that proposed in this work with the same purpose. The procedure for the Ouyang and Li method was based on using the developed analytical expression for estimating the G_{II}-δ_s curve, followed by differentiation of a polynomial fitting curve to produce the shear cohesive law. Only one specimen was compared for each adhesive, and only the results for the adhesives Araldite® AV138 and Sikaforce® 7752 are presented here, although the agreement between methods is identical for the three adhesives. Figure 14 shows the G_{II} – δ_s comparison between the two methods (the Araldite® AV138 curve is in secondary axis for a clearer visualization). The curves are practically overlapped for both adhesives, with a difference in the steady-state values, which provide the measurement of G_{IIC}, of −1.4 % (Araldite® AV138) and 0.9 % (Sikaforce® 7752). Figure 15 compares the shear cohesive laws for the same specimens of Fig. 14, considering the two methods. The CZM laws are virtually indistinguishable, although with minor variations in t_s^0 (−1.9 % for the Araldite® AV138 and 1.0 % for the Sikaforce® 7752). It is thus concluded that the two methods are quite similar in which regards to the output result.

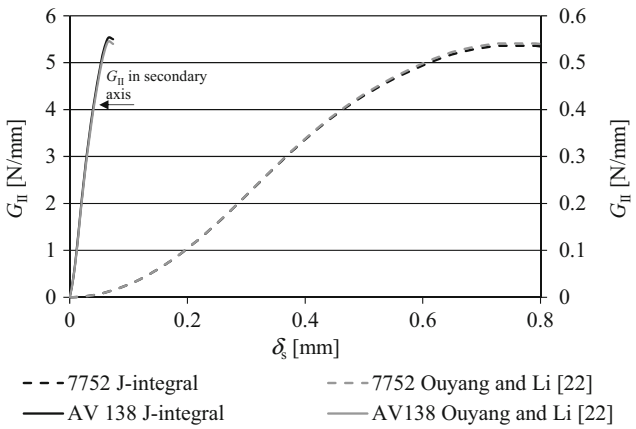

Fig. 14 G_{II} – δ_s comparison between the current *J*-integral formulation and the nonlinear solution of Ouyang and Li [22]: Araldite® AV138 and Sikaforce® 7752

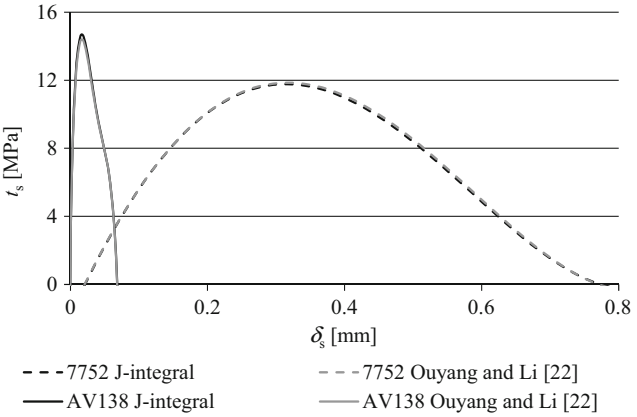

Fig. 15 CZM law comparison between the current *J*-integral formulation and the nonlinear solution of Ouyang and Li [22]: Araldite® AV138 and Sikaforce® 7752

Conclusions

This work addressed the calculation of G_{IIC} of different types of adhesives, considering the ENF test. The tested methods were the CCM, DBT, CBT, CBBM and *J*-integral, with the latter enabling the estimation of the shear CZM law of the adhesives. All methods showed a good agreement between specimens of a given adhesive. However, between methods the CBT showed smaller values of G_{IIC} (approximately 17 %). Comparing time requirements between methods, the CCM, DBT and CBT need the measurement of *a* during the tests,

oppositely to the CBBM. Apart from this, the CCM involves fitting of the $C=f(a)$ curves and derivation. Application of the J-integral, although allowing the estimation of the CZM law by differentiation of the $G_{II}=f(\delta_s)$ curve, is based on the measurement of δ_s, which requires a high-precision technique on account of the very small values of this parameter up to crack initiation. However, it has the big advantage of providing complete data (in this case in shear) for strength prediction by CZM modelling. The shear CZM laws of the adhesives obtained by the J-integral confirmed the brittle behaviour of the Araldite® AV138 in shear, which can be represented by a triangular CZM law. The Araldite® 2015 and Sikaforce® 7752 revealed a much higher degree of ductility in shear. Under these circumstances, the trapezoidal law enabled a very good fit of the experimental data. Together with tensile characterization data of these adhesives (the tensile laws for the Araldite® AV138 and 2015 are available in reference [39]) and mixed-mode damage initiation and propagation criteria, it is possible to predict the strength of bonded joints under generic loading conditions by CZM modelling.

Acknowledgments The authors would like to thank Sika® Portugal for supplying the adhesive.

References

1. da Silva LFM, Öchsner A, Adams RD (eds) (2011) Handbook of adhesion technology. Springer, Heidelberg
2. Klarbring A (1991) Derivation of a model of adhesively bonded joints by the asymptotic expansion method. Int J Eng Sci 29:493–512. doi:10.1016/0020-7225(91)90090-P
3. Campilho RDSG, Banea MD, Neto JABP, da Silva LFM (2013) Modelling adhesive joints with cohesive zone models: effect of the cohesive law shape of the adhesive layer. Int J Adhes Adhes 44:48–56. doi:10.1016/j.ijadhadh.2013.02.006
4. Andersson T, Stigh U (2004) The stress–elongation relation for an adhesive layer loaded in peel using equilibrium of energetic forces. Int J Solids Struct 41:413–434. doi:10.1016/j.ijsolstr.2003.09.039
5. Adams R, Comyn J, Wake W (1997) Structural adhesive joints in engineering, 2nd edn. Chapman and Hall, Abingdon
6. Ripling E, Mostovoy S, Patrick R (1964) Application of fracture mechanics to adhesive joints. ASTM STP 360:5–19
7. Zhu Y, Liechti KM, Ravi-Chandar K (2009) Direct extraction of rate-dependent traction-separation laws for polyurea/steel interfaces. Int J Solids Struct 46:31–51. doi:10.1016/j.ijsolstr.2008.08.019
8. Dugdale DS (1960) Yielding of steel sheets containing slits. J Mech Phys Solids 8:100–104. doi:10.1016/0022-5096(60)90013-2
9. Barenblatt GI (1962) The mathematical theory of equilibrium cracks in brittle fracture. Adv Appl Mech 7:55–129. doi:10.1016/s0065-2156(08)70121-2
10. Tvergaard V, Hutchinson JW (1993) The influence of plasticity on mixed-mode interface toughness. J Mech Phys Solids 41:1119–1135. doi:10.1016/0022-5096(93)90057-M
11. de Moura MFSF, Gonçalves JPM, Chousal JAG, Campilho RDSG (2008) Cohesive and continuum mixed-mode damage models applied to the simulation of the mechanical behaviour of bonded joints. Int J Adhes Adhes 28:419–426. doi:10.1016/j.ijadhadh.2008.04.004
12. Campilho RDSG, Banea MD, Neto JABP, da Silva LFM (2012) Modelling of single-lap joints using cohesive zone models: effect of the cohesive parameters on the output of the simulations. J Adhes 88:513–533. doi:10.1080/00218464.2012.660834
13. Lee MJ, Cho TM, Kim WS, Lee BC, Lee JJ (2010) Determination of cohesive parameters for a mixed-mode cohesive zone model. Int J Adhes Adhes 30:322–328. doi:10.1016/j.ijadhadh.2009.10.005
14. de Moura MFSF, Campilho RDSG, Gonçalves JPM (2008) Crack equivalent concept applied to the fracture characterization of bonded joints under pure mode I loading. Compos Sci Technol 68:2224–2230. doi:10.1016/j.compscitech.2008.04.003
15. de Moura MFSF, Campilho RDSG, Gonçalves JPM (2009) Pure mode II fracture characterization of composite bonded joints. Int J Solids Struct 46:1589–1595. doi:10.1016/j.ijsolstr.2008.12.001
16. Campilho RDSG, de Moura MFSF, Pinto AMG, Morais JJL, Domingues JJMS (2009) Modelling the tensile fracture behaviour of CFRP scarf repairs. Compos Part B 40:149–157. doi:10.1016/j.compositesb.2008.10.008
17. Flinn BD, Lo CS, Zok FW, Evans AG (1993) Fracture-resistance characteristics of a metal-toughened ceramic. J Am Ceram Soc 76:369–375. doi:10.1111/j.1151-2916.1993.tb03794.x
18. Mello AV, Liechti KM (2006) The effect of self-assembled monolayers on interfacial fracture. J Appl Mech 73:860–870. doi:10.1115/1.1940662
19. Pandya KC, Williams JG (2000) Measurement of cohesive zone parameters in tough polyethylene. Polym Eng Sci 40:1765–1776. doi:10.1002/pen.11308
20. Campilho RDSG, Moura DC, Gonçalves DJS, da Silva JFMG, Banea MD, da Silva LFM (2013) Fracture toughness determination of adhesive and co-cured joints in natural fibre composites. Compos Part B 50:120–126. doi:10.1016/j.compositesb.2013.01.025
21. Leffler K, Alfredsson KS, Stigh U (2007) Shear behaviour of adhesive layers. Int J Solids Struct 44:530–545. doi:10.1016/j.ijsolstr.2006.04.036
22. Ouyang Z, Li G (2009) Nonlinear interface shear fracture of end notched flexure specimens. Int J Solids Struct 46:2659–2668. doi:10.1016/j.ijsolstr.2009.02.011
23. Ji G, Ouyang Z, Li G (2011) Effects of bondline thickness on Mode-II interfacial laws of bonded laminated composite plate. Int J Fract 168:197–207. doi:10.1007/s10704-010-9571-9
24. Ji G, Ouyang Z, Li G (2012) Local interface shear fracture of bonded steel joints with various bondline thicknesses. Exp Mech 52:481–491. doi:10.1007/s11340-011-9507-y
25. Carlberger T, Stigh U (2010) Influence of layer thickness on cohesive properties of an epoxy-based adhesive—an experimental study. J Adhes 86:816–835. doi:10.1080/00218464.2010.498718
26. Marzi S, Biel A, Stigh U (2011) On experimental methods to investigate the effect of layer thickness on the fracture behavior of adhesively bonded joints. Int J Adhes Adhes 31:840–850. doi:10.1016/j.ijadhadh.2011.08.004
27. Stigh U, Alfredsson K, Biel A (2009) Measurement of cohesive laws and related problems. In: Proceedings of the ASME Int Mech Eng Congress and Exposition
28. Campilho RDSG, Banea MD, Pinto AMG, da Silva LFM, de Jesus AMP (2011) Strength prediction of single- and double-lap joints by standard and extended finite element modelling. Int J Adhes Adhes 31:363–372. doi:10.1016/j.ijadhadh.2010.09.008
29. Faneco TMS (2014) Caraterização das propriedades mecânicas de um adesivo estrutural de alta ductilidade, MSc Thesis, Instituto Superior de Engenharia do Porto, Portugal
30. Compston P, Jar PYB, Burchill PJ, Takahashi K (2001) The effect of matrix toughness and loading rate on the mode-II interlaminar fracture toughness of glass-fibre/vinyl-ester composites. Compos Sci Technol 61:321–333. doi:10.1016/S0266-3538(00)00226-8

31. Elmarakbi A (ed) (2014) Advanced composite materials for automotive applications: Structural integrity and crashworthiness. Wiley, Hoboken
32. Wang Y, Williams JG (1992) Corrections for mode II fracture toughness specimens of composite materials. Compos Sci Technol 43:251–256. doi:10.1016/0266-3538(92)90096-L
33. Rice JR (1968) A path independent integral and the approximate analysis of strain concentration by notches and cracks. J Appl Mech 35:379–386. doi:10.1115/1.3601206
34. Ameli A, Papini M, Schroeder JA, Spelt JK (2010) Fracture R-curve characterization of toughened epoxy adhesives. Eng Fract Mech 77:521–534. doi:10.1016/j.engfracmech.2009.10.009
35. Ji G, Ouyang Z, Li G, Ibekwe S, Pang SS (2010) Effects of adhesive thickness on global and local mode-I interfacial fracture of bonded joints. Int J Solids Struct 47:2445–2458. doi:10.1016/j.ijsolstr.2010.05.006
36. Campilho RDSG, Moura DC, Banea MD, da Silva LFM (2014) Adherend thickness effect on the tensile fracture toughness of a structural adhesive using an optical data acquisition method. Int J Adhes Adhes 53:15–22. doi:10.1016/j.ijadhadh.2014.01.015
37. Pelfrene J, Van Dam S, Paepegem V (2015) Numerical analysis of the peel test for characterisation of interfacial debonding in laminated glass. Int J Adhes Adhes 62:146–153. doi:10.1016/j.ijadhadh.2015.07.010
38. Desai CK, Basu S, Parameswaran V (2015) Determination of traction separation law for interfacial failure in adhesive joints at different loading rates. J Adhes. doi:10.1080/00218464.2015.1046986
39. Constante CJ, Campilho RDSG, Moura DC (2015) Tensile fracture characterization of adhesive joints by standard and optical techniques. Eng Fract Mech 136:292–304. doi:10.1016/j.engfracmech.2015.02.010